Back to Session Subjects

AERODYNAMIC INVESTIGATIONS OF UNSTEADY FLOW PAST ROBIN HELICOPTER WITH FOUR-BLADED ROTOR IN FORWARD-FLIGHT

Hongyi Xu[1], and Steve Zhang[2]

[1, 2] Institute for Aerospace Research, National Research Council, NRC
1200 Montreal Road, Ottawa, Ontario, Canada, K1A 0R6
e-mail: hongyi.xu@nrc-cnrc.gc.ca

Key words: RoBin Helicopter, Unsteady Rotor Flow, Forward Flight, CFD method

Abstract: The current paper presents the unsteady aerodynamic performance of the RoBin helicopter with a four-bladed rotor in a forward-flight condition. The investigation was performed using Computational Fluid Dynamic (CFD) method implemented in CFD-FASTRAN. The flow past the RoBin fuselage and the four-bladed rotor was simulated in a time accurate fashion using the Chimera moving grid technique and the four blades were equipped with the motions of rotation and cyclic pitching. The Chimera moving grid capability was validated previously through the numerical simulations of the unsteady flows past a two-bladed rotor and a four-bladed rotor in forward flights. Additionally, computation results of an isolated RoBin fuselage were in good agreement with experimental data.

Following the validations, the aerodynamic performance of the RoBin helicopter with a four-bladed rotor in a forward flight was investigated. The four-bladed rotor considered in the present study was experimentally tested at the NASA Langley Research Center. The blade had a linear twist of -8° and a coning angle of 1.5°. Cyclic pitching motion was applied to each of the four blades. The computational results were compared with the experimental measurements of inflow ratios at a variety of azimuth stations, which showed a promising agreement. The aerodynamic performance of the rotor was further studied by analyzing the blade thrust coefficient history. The flow interaction between the rotor and fuselage was investigated by tracking the pressure coefficient variations on the fuselage surface as a function of the rotation angle of the rotor blades. The current study indicates that Chimera moving grid method provides a feasible and practical way for investigating the complex flows past helicopter.

INTRODUCTION

Flows past rotary-wing flight vehicles involve a variety of complex aerodynamic phenomena, which poses a grand challenge to the rotorcraft Computational Fluid Dynamic (CFD) community for their modeling and simulation. These complex aerodynamic phenomena include: (1) advancing blade transonic flow; (2) retreating blade stall and separated flow; (3) complex blade-tip vortex system and (4) rotor-fuselage flow interactions. These flow phenomena involve the physics of turbulence, unsteadiness, separation, interaction and vibration as well as acoustics. So far, several of these phenomena, such as advancing blade transonic flow, have been successfully addressed and simulated based on the existing CFD models, such as Reynolds Averaged Navier-Stokes (RANS) or Euler methods. A wide variety of these complicated flow phenomena, most of them related with unsteady flow separations, are yet waiting for more advanced and next-generation CFD models, such as Detached Eddy Simulation (DES) or Large Eddy Simulation (LES).

In addition to the challenges of modeling the complicated flow physics, the grid generation for rotorcraft flight vehicles poses a unique challenge to the rotorcraft CFD community. Because of the rotation of each rotor blade and its associated complex pitching and flapping motions, conventional multiblock grid generation using a fixed grid topology is no longer a suitable strategy. It cannot account for the meshing around the moving blades, which is necessary to resolve the near-blade flow features. In this regard, several alternative methodologies have emerged to overcome the deficiencies of the conventional grid generation methods. The Chimera moving grid technique, introduced by Steger et al. [1], is one approach that has received increased attention in rotor flow-field simulations. This technique has been widely utilized in a variety of rotorcraft applications, which include multi-bladed rotors in hover and forward flight [2-6], and unsteady rotor-fuselage interaction [7].

To build a capability for the numerical simulation of unsteady helicopter rotor flow, the Institute for Aerospace Research, National Research Council Canada (IAR/NRC) acquired the commercial CFD-FASTRAN package, which includes the grid generator of CFD-GEOM, the flow solver of CFD-FASTRAN and the data post-processing code CFD-VIEW. The Chimera moving grid capability of the package was carefully tested for a two-bladed simple rotor in forward flight conditions as reported in Xu et al. [8]. The validation was conducted at a variety of flow conditions and various rotor blade geometries. The pressure distributions were compared against the experimental data of Caradonna et al. [9] and a number of previous Euler calculations by Chen et al. [10].

To extend the Chimera capability beyond the simple model rotor simulation to realistic unsteady rotor simulation with blade motion including complex motion schedules, an isolated four-bladed rotor in forward flight [11] was investigated. The four-bladed rotor was experimentally tested at the Langley Research Center of NASA [12]. The experiment was conducted with a RoBin fuselage along with the rotor. Computationally, the blade motion, which is expressed as a function of the azimuth rotation angle, was implemented by cyclic pitching for each of the blades. The induced inflow ratios at a number of azimuth radial stations were compared with experimental measurements and reasonable agreements were obtained.

Following these validations, the aerodynamic performance of the RoBin helicopter with a four-bladed rotor in a forward flight, as reported in [12], was investigated and is the subject of the current paper. As a first step, the CFD-FASTRAN flow solver was tested using the flow past an isolated RoBin fuselage, the measurement of which was provided by Chaffin et al. [13]. Experimental and calculated surface pressure coefficients were compared. Then in the second step of the investigation, the rotor was included. The blade had a linear twist of -8° and a coning angle of 1.5°. The cyclic pitching motion, as given by the experiment, was applied for each of the four blades. The computational results were compared with the experimental measurements of induced inflow ratios at a variety of azimuth stations. The overall aerodynamic performance of the rotor was studied by analyzing the blade thrust coefficient history. The flow interaction between the rotor and fuselage was investigated by tracking the pressure coefficient variations on fuselage surface with the rotation of rotor blades.

1. Governing Equations and Numerical Algorithm

The governing equations, as implemented in CFD-FASTRAN, can be derived by applying the mass and momentum balance relations to a control volume V with a boundary ∂V in a Cartesian coordinate system. The control volume moves and deforms according to the volume surface velocity vector $\vec{v}_g$. The integral form of the unsteady compressible Navier-Stokes equations can then be written as:

(1) Continuity equation

$$\frac{d}{dt}\iiint_V \rho dV + \iint_{\partial V} \rho(\vec{v} - \vec{v}_g)\cdot\vec{n}dA = 0 \tag{1.1}$$

(2) Momentum and energy equations

$$\frac{d}{dt}\iiint_V Q dV + \iint_{\partial V} (\vec{F}_C - Q\vec{v}_g - \vec{F}_D)\cdot\vec{n}dA = \iiint_V S dV \tag{1.2}$$

where Q is the conservative variables vector, $Q = (\rho u, \rho v, \rho w, \rho E)^T$, $\vec{F}_c$ is the convective (inviscid) flux and $\vec{F}_D$ is the diffusive (viscous) flux, $\vec{v}_g$ is the volume surface velocity and S is the source term vector.

In the current investigation, the flow is assumed to be governed by the Euler equations ($\vec{F}_D = 0$). This assumption significantly alleviates the grid density requirement near the blade surfaces and, therefore, greatly reduces the CPU time and memory requirement of the simulation. More detailed description of the governing equations can be found in the theory manual of CFD-FASTRAN [14].

The governing equations (1.1) and (1.2) are spatially discretized using the finite volume method. By applying the integral formulations of Eqs (1.1) and (1.2) to a finite control volume and using the divergence theorem, the following discretized form of the governing equations can be derived, where: $\vec{n}$ is the cell face normal, subscription f denotes the surface indices of the control volume, ΔA is the surface area of the control volume, the Q represents the conservative variables vector $Q = (\rho, \rho u, \rho v, \rho w, \rho E)^T$; $\vec{F} = \vec{F}_c - Q\vec{v}_g$ stands for the convective-moving flux and $\partial\vec{F}/\partial Q$ and $\partial S/\partial Q$ are the flux Jacobian and source Jacobian, respectively.

$$\begin{aligned} &\frac{\Delta Q}{\Delta t}\Delta V^{n+1} + \sum_{f=1}^{N_f}\left[\left.\frac{\partial\vec{F}}{\partial Q}\right|^n \Delta Q \bullet \vec{n}_f^{n+1}\Delta A_f^{n+1}\right] - \\ &\left(\Delta V^{n+1}\left.\frac{\partial S}{\partial Q}\right|^n\right)\Delta Q = S\Delta V^{n+1} - \sum_{f=1}^{N_f}\vec{F}_f^n \bullet \vec{n}_f^{n+1}\Delta A_f^{n+1} + Q^n\delta V^n \end{aligned} \tag{1.3}$$

The flux vector and the flux Jacobians are evaluated using Roe's approximate Riemann solver, which is a flux difference scheme. High order spatial accuracy is achieved in CFD-FASTRAN using various gradient limiters [14]. The Osher-Chakravarthy limiter is used in the current investigation to capture better shockwaves since this limiter can produce a third-order accuracy.

The time marching algorithm used in the current application is the Jacobi iterative implicit scheme, in which only the nearest neighbors to the center cell are taken into consideration. This scheme has first-order accuracy in time.

The WIND code [15], used in solving the flow of isolated RoBin fuselage in current application, is a product of the NPARC Alliance, a partnership between the NASA Glenn Research Center (GRC) and the USAF Arnold Engineering Development Center (AEDC). The flow solver (WIND) is based-on the Euler and N-S equations of fluid mechanics, along with the supporting equations governing turbulent and chemical reacting phenomena. The flow equations are discretized using finite difference scheme with second-order accuracy.

2. Grid Generation and Chimera Grids

Figure 1 presents the Chimera grid topology for the RoBin helicopter at zero degree blade rotational angle configuration ($\psi = 0^\circ$ where ψ is the angle between the rotor blade and the x-axis positive down-stream), which includes the background cylindrical grid, the C-grid for rotor-blade and the O-grid for RoBin fuselage. Figure 2 gives the detailed grid arrangement near the RoBin fuselage and rotor blades. The meshes are generated by CFD-GEOM [14] and are based on the CAD geometries of rotor-blades and RoBin fuselage. The background grid contains two half cylindrical domains, with the radius of the domain at $2.8m$ and the height of the domain at $5.6m$. 54 mesh points are used in the radial direction, 60 points in the circumferential direction and 87 points in the height direction. The mesh around fuselage uses two blocks with an O-grid topology and the grid size of $I \times J \times K = 30 \times 137 \times 117$. The rotor blades are gridded using a C-H grid topology with two blocks around each blade and the grid size at $I \times J \times K = 63 \times 30 \times 72$ for each block. A total of 103 mesh points are distributed along the profile of the blade in the chordwise direction. About 2.6 million grid points is used for the entire RoBin helicopter.

3. Cyclic Motions of the Four-bladed Rotor

In the current application, the relative rotating and cyclic-pitching motions of the blades are prescribed by assigning the corresponding grid velocity to the blade Chimera domain (see reference [14] for more details).

The individual blade is generated in an untapered planform, using the NACA 0012 airfoil profile. The rotor blade rotational speed was set to 2113 rpm to match the experiments conducted at NASA [12]. The unsteady computations were continuously marched in time using a small time step of 1.184×10^{-5} sec, which corresponds to an incremental rotational angle of 0.15°. The radius of the rotor is 0.86 m, the root cutout radius is 0.20 m. The blade chord length is 0.066 m, which gives a blade aspect ratio of 13.03. A linear twist of -8° is applied in the radial direction for each rotor blade. The cyclic-pitching motion is implemented for each of the blades, which is expressed as a function of the azimuth rotational angle ψ by the first two harmonic terms of the following Fourier series: $\theta = A_0 - A_1 \cos\psi - B_1 \sin\psi$. Here, ψ is measured from the downwind horizontal line, as referenced in Figure 3, in the counter-clockwise direction when viewed from above. The values of the three constants are $A_0 = 9.37^\circ$, $A_1 = -1.11^\circ$ and $B_1 = 3.23^\circ$. The local angle of attack of the blades, including the cyclic pitching and the blade twist, is presented in Figure 3 as the function of the azimuth angle ψ. A coning angle of 1.5° is implemented and a shaft angle of -3.0° is considered in the simulation. No flapping and lead/lag motions are included in the current simulation.

4. Presentation and discussion of results

4.1 Flow past isolated RoBin fuselage

The simulation for flows past isolated RoBin fuselage was performed to test code accuracy in predicting the flow past a helicopter fuselage. Chaffin and Berry [13] report the experimental measurements of surface pressure coefficients on RoBin fuselage, which included comparisons with numerical predictions using the potential code VSAERO and the thin-layer Navier-Stokes code CFL3D. In the present study, the flow past RoBin fuselage was investigated using CFD-FASTRAN [14] with finite-volume scheme and WIND [15] with finite-difference scheme. The flow conditions set the freestream

Mach number to 0.062 and angle of attack at 0.0°, a condition reported in Ref. [13]. Figure 4 presents the station-cuts where the pressure coefficients are taken to compare with the experimental measurements. Figure 5 gives the numerical predictions and the comparison with experimental data at a total of fourteen station-cuts in the streamwise direction from the nose to the rear part of the fuselage. These comparisons indicate that the WIND results agree better in the nose region with experimental data and CFD-FASTRAN results are closer to experiment in the rear part of the fuselage. In general, both predictions agree with measurement data reasonably well and these validations provide a certain level of confidence in simulating the subsonic fully attached flows. Applying the code to simulate more complex flow configuration, such as RoBin helicopter, need to be further validated.

4.3 Simulation results of RoBin helicopter

The RoBin fuselage with a four-bladed rotor is a typical generic helicopter model, which has received extensive investigations. For example, this model was experimentally tested at the Langley Research Center of NASA [12] as early as 1988. More recently, a wind tunnel test of this helicopter model with an independently mounted rotor was conducted and reported in [16]. The simulation results obtained in the current paper were based on the flow conditions reported in [12]. The experiment was operated at an advance ratio of 0.15. The oncoming flow was thus 28.65 m/s.

4.3.1 Rotor integral performance

Based on the definitions provided in [12], the rotor thrust C_T and torque C_Q coefficients are defined as: $C_T = T/\left(\rho A V_{tip}^2\right)$ and $C_Q = Q/\left(\rho A R V_{tip}^2\right)$, where T is the rotor thrust (total lift force) and Q is the rotor torque (total moment in y direction); ρ is the density of fluid, $A = \pi R^2$ is the rotor rotational area and $V_{tip} = \Omega R$ is the blade tip velocity. Likewise, the blade thrust coefficient and blade torque coefficient can be defined as the blade lift force nondimensionalized by $\rho A V_{tip}^2$ and the blade torque non-dimensionalized by $\rho A R V_{tip}^2$, respectively.

The time instant histories of blade thrust coefficients and torque coefficients for three rotor revolutions are presented in Figures 6 and 7. The four blades follow the same sinusoidal variation pattern in one rotor rotation. From the blade thrust coefficient history in Figure 10, it can be seen that, by following the blade-1 thrust coefficient variation (black dot curve), the blade at 90° rotational angle experiences the largest peak aerodynamic load since this blade is on the advancing side and sees the largest relative velocity. The second peak aerodynamic load occurs at the blade rotational angle of 270° where the blade sees the larger angle of attack, as indicated in Figure 3. The variation of torque coefficient on blade-1 in one rotational cycle presents one high peak occurring at a rotational angle between 240° and 270° and one low peak at a rotational angle between 30° and 60°.

Figures 8 and 9 present the time histories of the total thrust and the total torque coefficients, respectively. The figures confirm that the periodicity of the flow was established after the second revolution. According to Ref. [12], these rotor performance parameters were at the values of $C_T = 0.0063$ and $C_Q = 0.00036$. The simulation predicted an averaged value of thrust coefficient $C_T = 0.00893$ and torque coefficient $C_Q = 0.000686$. These averaged coefficients were calculated based on the instantaneous values between the rotation angles of 1080° and 1440°. Compared with experimental values, the current simulation over-predicted the thrust and torque coefficients by about 41% and 90%, respectively. The over-prediction of the pressure and torque coefficients may be attributed to neglecting viscous effects in the current simulation, since the Euler equations are not capable of capturing the flow separations and hence the dynamic stall phenomena, particular for the blades on the retreating side.

4.3.2 Rotor induced inflow ratio

The induced inflow ratio normal to tip path plane is defined as $\mu_i = v / V_{tip}$ where v is velocity component normal to the tip path plane, and $V_{tip} = \Omega R$ is the rotor blade tip velocity with Ω and R being the rotational speed and rotor radius, respectively. Experimental measurements were made at azimuth increments of 30° from $\Psi = 0^\circ$ to $\Psi = 360^\circ$, excluding 120° and 270° as presented in Figure 10, at three inches above the plane formed by the tips of the rotor blades. Measurements were made at radial locations ranging from $r/R = 0.2$ to $r/R = 1.1$, with the majority of the measurement locations concentrated toward the outboard portion of the rotor rotation plane. Figure 11 gives the numerical predictions of induced inflow ratio at ten azimuthal stations, which are compared with experimental measurements. The results from the current simulation generally agree with the distributions of induced inflow ratio obtained from the experimental measurement for most of the azimuth stations. At some azimuth stations, such as $\Psi = 60^\circ$, $\Psi = 90^\circ$ and $\Psi = 150^\circ$, the induced inflow ratios from the current simulation are over-predicted compared with experimental measurements, which is consistent with the higher values of thrust coefficient as predicted by the present calculation when compared against the measurements.

4.3.3 Rotor blade pressure distribution

The pressure coefficient for the rotor in forward flight conditions is defined as: $C_p = \dfrac{p - p_\infty}{1/2\,\rho_\infty (\Omega R)^2}$.

Figure 12 presents the C_p distributions on each of the four blade surfaces at rotational azimuth angle of zero degree. The C_p distributions at three typical relative radial stations, namely: $r/R = 0.34$, $r/R = 0.64$ and $r/R = 0.92$, are extracted out and are plotted in Figures 13. Generally, the patterns of the C_p distributions exhibit the flow behavior around an airfoil. On the pressure surface, C_p quickly rises to its high peak value around the leading edge of the blade and then gradually decreases along the rest of the chord length. On the suction surface, C_p sharply decreases to its low peak value around the leading edge and then gradually rises along the rest of the chord length of the rotor blade. It can be seen that although the blade has a -8° twist, the aerodynamic loads on the rotor blade surfaces generally increase from the rotor root region to the rotor tip region because of the increase of local relative velocity. The pressure distributions in Figure 13 are qualitative presentation of flow behaviors. In general, the C_p presents reasonable distributions and however, no experimental data are available for comparison.

4.3.4 RoBin fuselage integral aerodynamic performance

The aerodynamic force on the RoBin fuselage surface was obtained by integrating the surface pressure and this force was projected into the three spatial directions, namely, f_x in the streamwise direction (x), f_y in the vertical direction (y) and f_z in the yaw direction (z). The integrated moment on the RoBin fuselage surface was generated with the origin point (rotor rotation center) selected as the reference point and this moment contained the three components (m_x m_y m_z) in the three spatial directions, respectively. Following the convention used in Ref [12], these force and moment components were non-dimensionalized using the characteristic force ($\rho A V_{tip}^2$) and moment ($\rho A R V_{tip}^2$), respectively, based on the blade-tip velocity and rotor disk area.

Figure 14 presents the integral force history for the RoBin fuselage. The fuselage is subjected to a positive averaged force (f_x=0.00007133) in the streamwise direction. Comparing the amplitudes of the fluctuations with other two directions, the fluctuation in the streamwise direction is much smaller, with the amplitude at about 0.000025. In the vertical direction (y), the downwash effect caused an averaged negative force (f_y=-0.00007821) on the fuselage. The amplitude of the fluctuation in vertical direction is quite bigger, which is at about 0.00015. In the yaw direction, the fuselage is subjected to an averaged positive force (f_z=0.00003279), which is caused by the sidewash effect of the rotor.

The fluctuation amplitude of this sidewash force is at about 0.000075, which is in between the fluctuation amplitudes in the other two directions. The averaged sidewash force is about twice smaller than the averaged forces in other two directions. In terms of force fluctuation amplitude, the downwash effect is the most dominant phenomenon.

The integral moment history is provided in Figure 15. Because of the rotor downwash effects, the moment component in the z direction (m_z) has a dominant averaged value of 0.00009010, which means that the downwash flow pushes the fuselage downward more strongly around the nose region than around the rear region. The fluctuation amplitude of m_y is about 0.00005. The rotor swirl (sidewash effects) generates a moment that makes the fuselage have a tendency to rotate in the positive y direction. The averaged m_y is equal to 0.00003637 and the fluctuation amplitude is about 0.00008. Since the sidewash exerts a positive averaged force in z direction, therefore, this force generates an averaged negative moment in x direction (m_x =-0.000003824), pretty smaller compared with the component in the other two directions, when the moment is calculated with the original point as the reference point.

5. Conclusions

In the current study, the simulation was extended to a RoBin helicopter flow with a four-bladed rotor moving with complex motion schedule. The induced inflow ratios from the current investigation were compared with experimental measurements and showed a reasonably good agreement for most of the azimuth stations. Some over-prediction of inflow ratios were found at three azimuth stations. The integral parameters, such as the thrust and torque coefficients, were over-predicted by about 41% and 91% compared with experiment, respectively. The pressure coefficient on the blade surface shows reasonable distribution, however, no experimental data were available for quantitative comparison. The analysis of the integral force and moment on the RoBin fuselage surface indicate that the downwash effect and sidewash effect play an important role in the force and moment being exerted on the fuselage, with downwash being the dominant factor. The current investigation is an initial effort towards applying the CFD-FASTRAN code to unsteady flow simulations past a real helicopter configurations, such as Bell 412 helicopter.

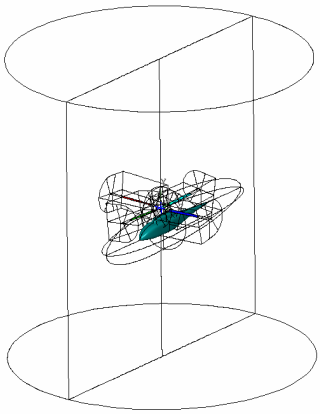

Figure 1: Grid topology for grids of background, RoBin fuselage and blades

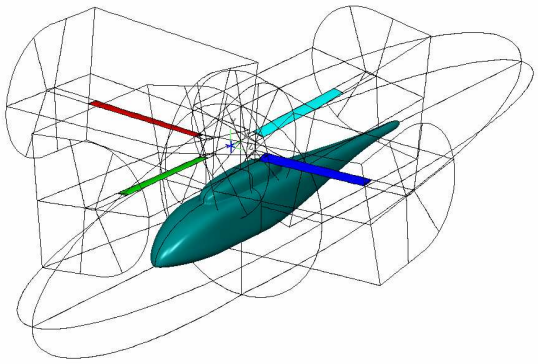

Figure 2: Detail grid arrangement around RoBin fuselage and rotor blades

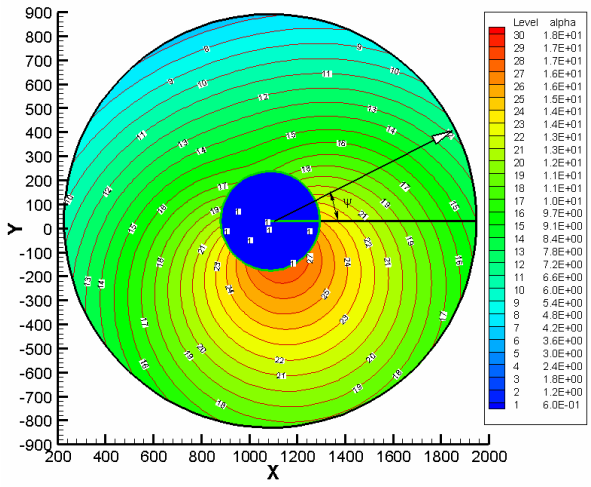

Figure 3: Angle of attack distribution on rotor rotating plane

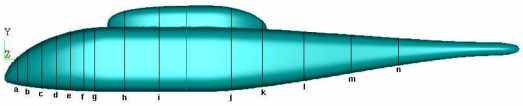

Figure 4: Station cuts on the surface of the Isolated RoBin fuselage for pressure coefficient comparison

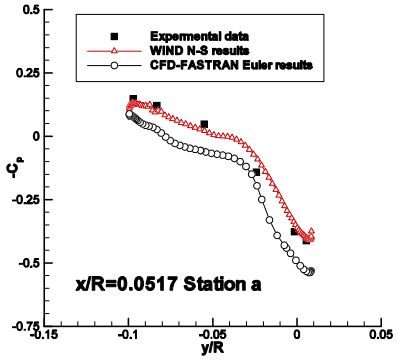

(a)

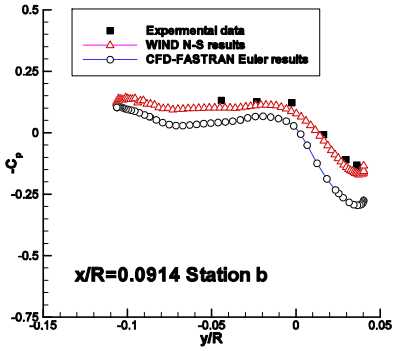

(b)

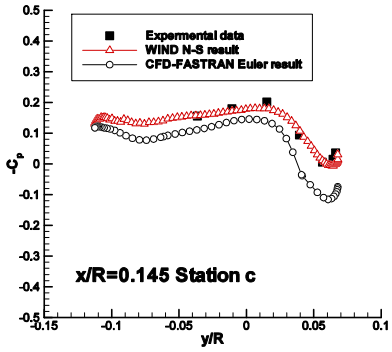

(c)

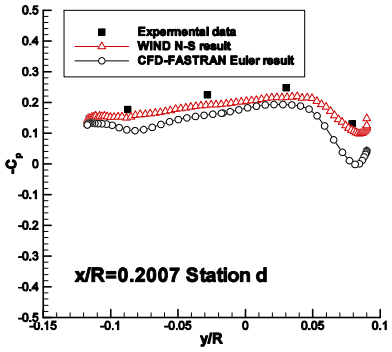

(d)

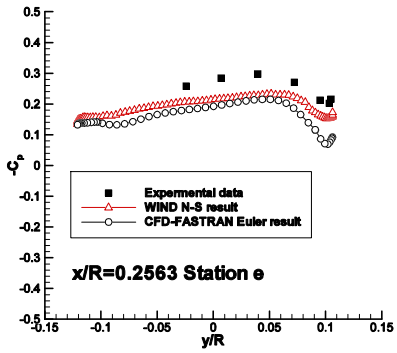
-Cp
y/R
Expermental data
WIND N-S result
CFD-FASTRAN Euler result
x/R=0.2563 Station e

(e)

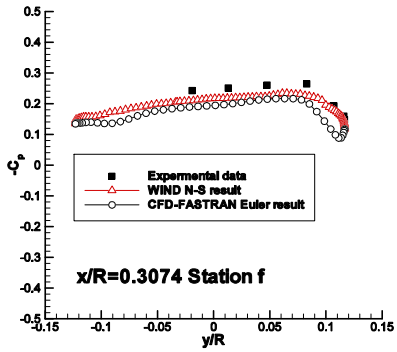
-Cp
y/R
Expermental data
WIND N-S result
CFD-FASTRAN Euler result
x/R=0.3074 Station f

(f)

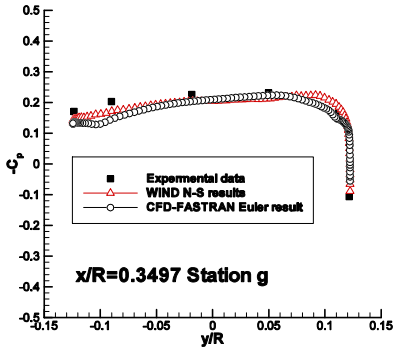
-Cp
y/R
Expermental data
WIND N-S results
CFD-FASTRAN Euler result
x/R=0.3497 Station g

(g)

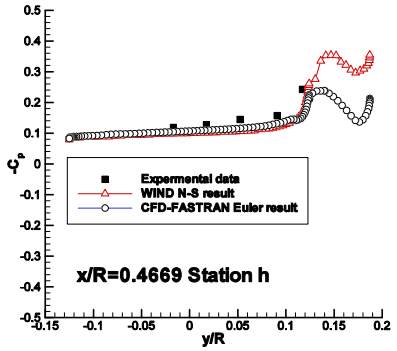
-Cp
y/R
Expermental data
WIND N-S result
CFD-FASTRAN Euler result
x/R=0.4669 Station h

(h)

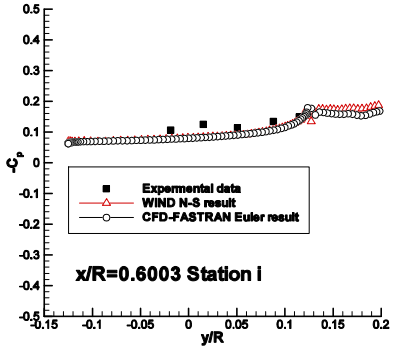
-Cp
y/R
Expermental data
WIND N-S result
CFD-FASTRAN Euler result
x/R=0.6003 Station i

(i)

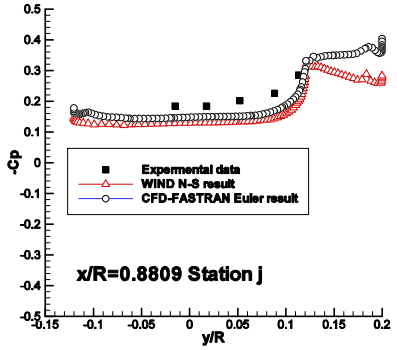
-Cp
y/R
Expermental data
WIND N-S result
CFD-FASTRAN Euler result
x/R=0.8809 Station j

(j)

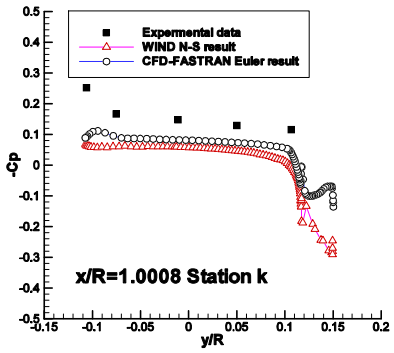

(k)

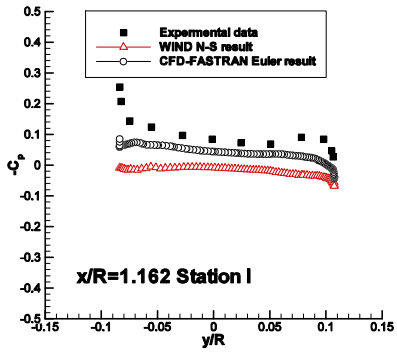

(l)

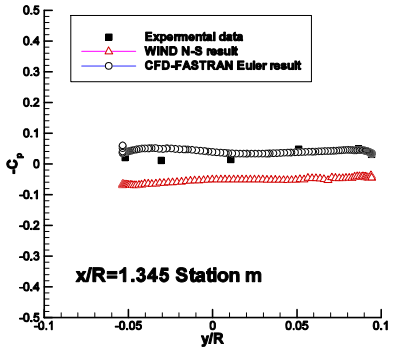

(m)

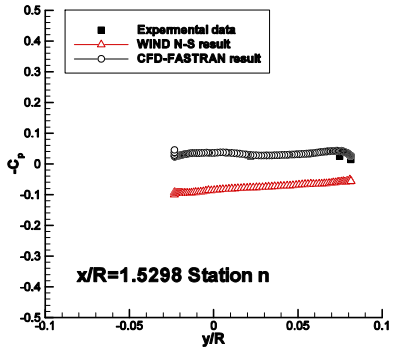

(n)

Figure 5: Pressure coefficient comparisons between numerical predictions and experimental measurements at various station-cuts on the RoBin fuselage surface

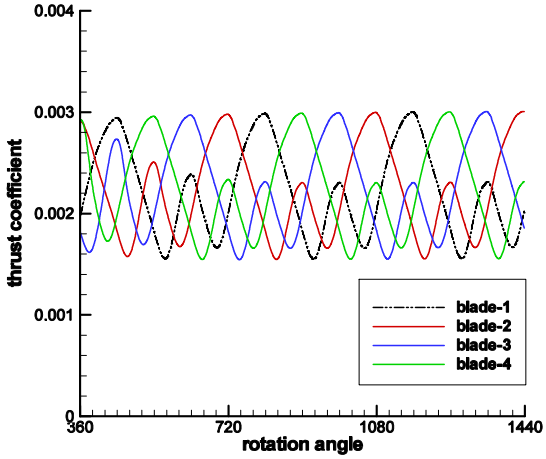

Figure 6:Variation of instantaneous thrust coefficients for individual rotor blade

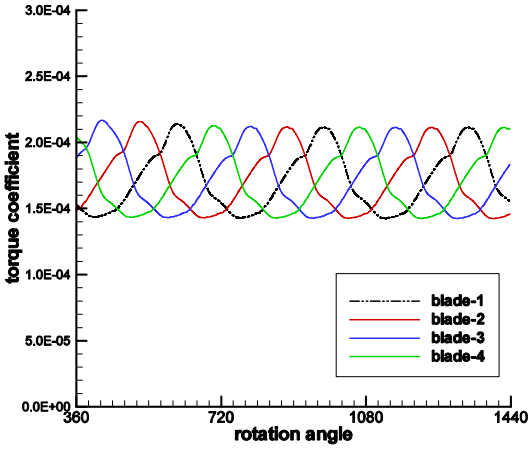

Figure 7: Variation of instantaneous torque coefficients for individual rotor blade

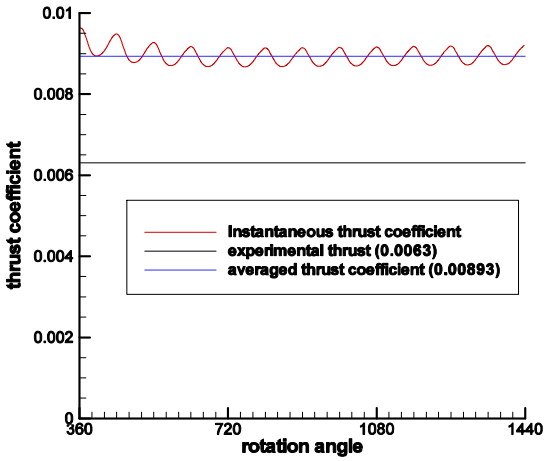

Figure 8: Instantaneous and averaged rotor thrust coefficient compared with experimental value

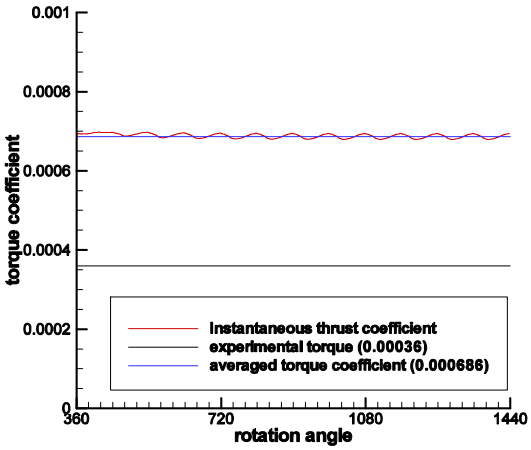

Figure 9: Instantaneous and averaged rotor torque coefficient compared with experimental value

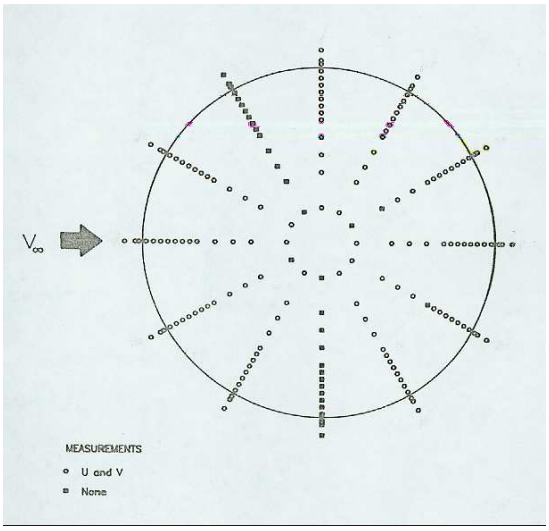

Figure 10:Locations of experimental inflow ratio measurements

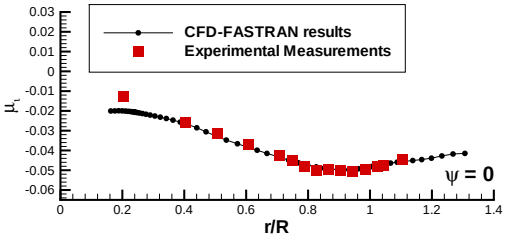

(a)

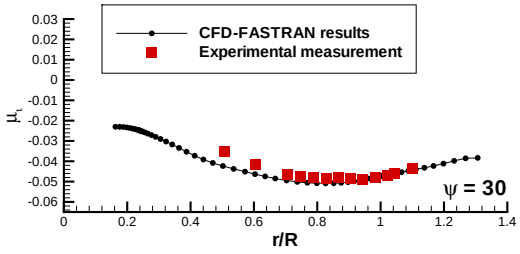

(b)

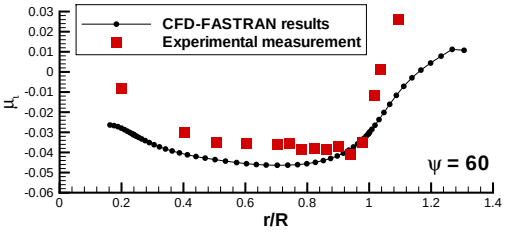

(c)

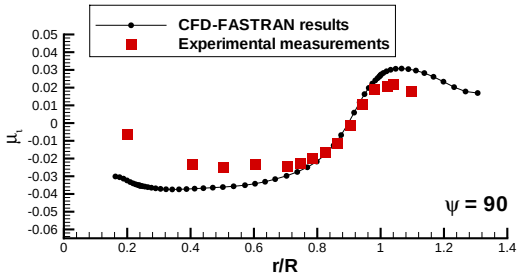

(d)

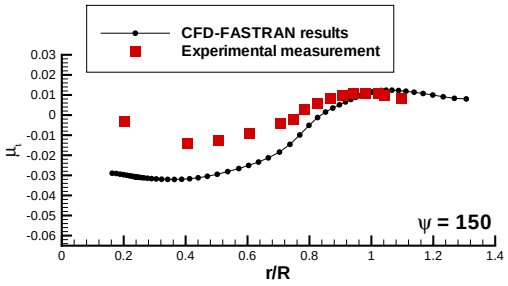

(e)

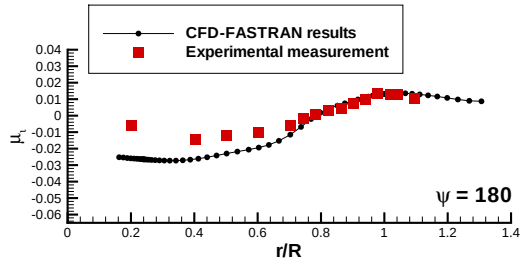

(f)

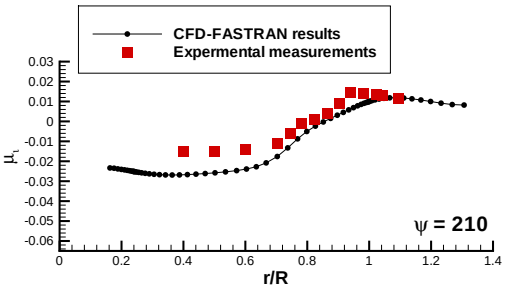

(g)

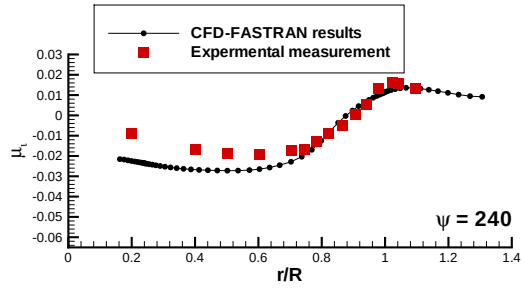

(h)

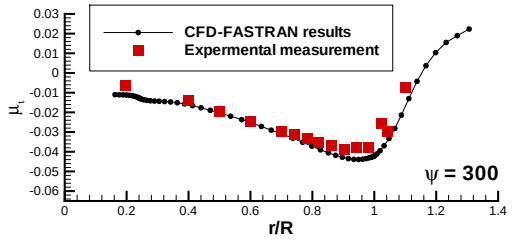

(i)

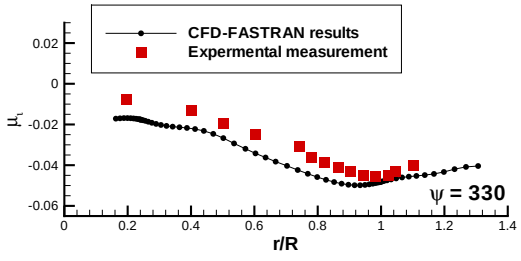

(j)

Figure 11:Comparison of induced inflow ratios between numerical prediction and experimental data

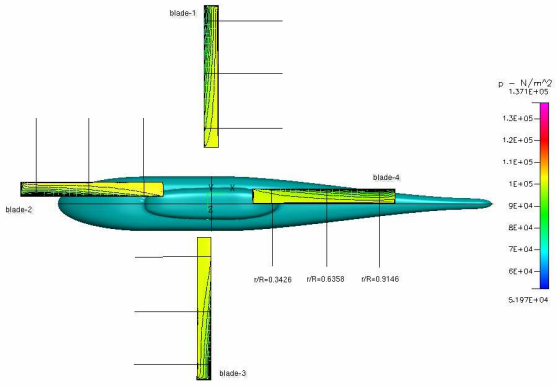

Figure 12: Global C_p distributions on the four blade surfaces at zero rotational angle

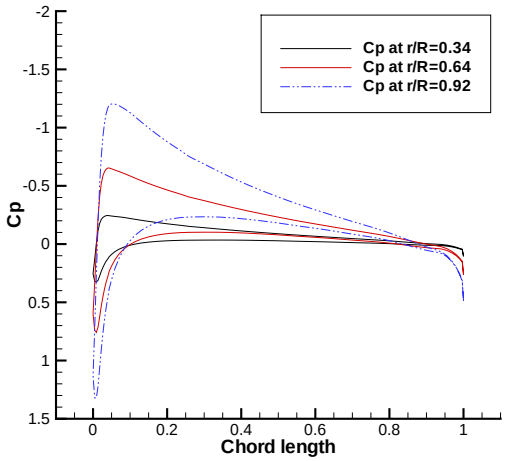

(Blade-1)

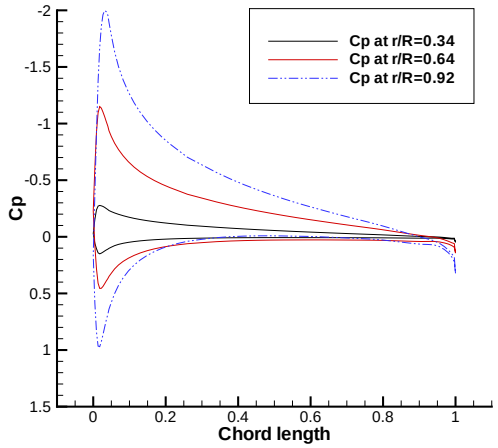

(Blade-2)

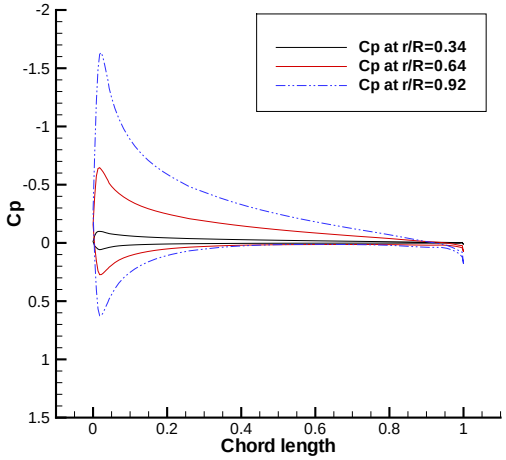

(Blade-3)

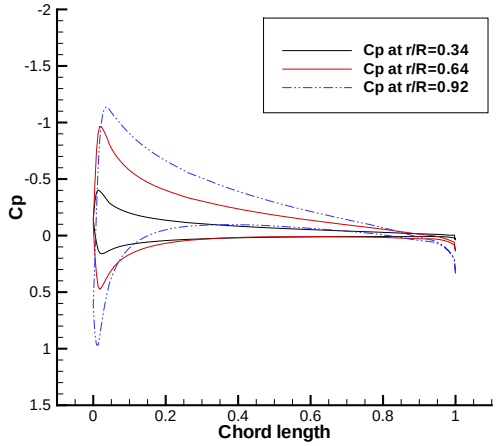

(Blade-4)

Figure 13: Pressure coefficient distributions on rotor blade at zero rotational angle

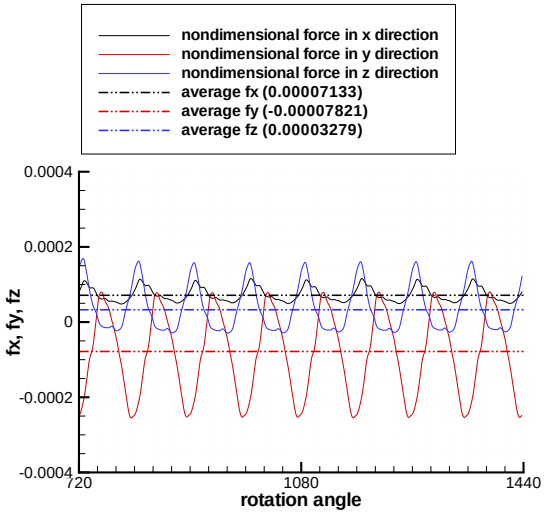

Figure 14: Integral force on RoBin fuselage

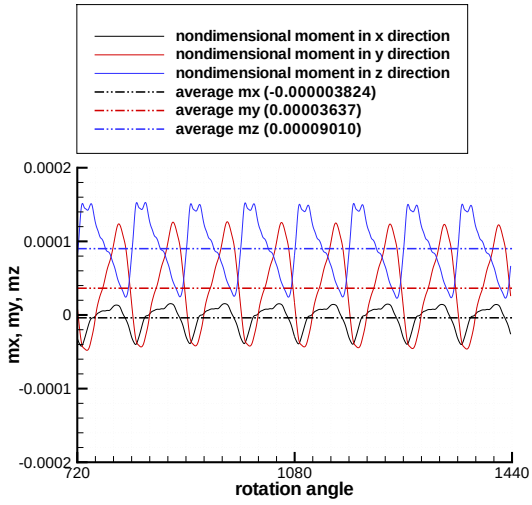

Figure 15: Integral moment on RoBin fuselage

REFERENCES

[1] J.L. Steger, F.C. Dougherty and J.A. Benek, "A Chimera Grid Scheme", ASME Mini symposium on advances in grid generation, Houston, 1993.

[2] K. Pahlke and J. Raddatz, "Flexibility Enhancement of Euler Codes for Rotor Flows by Chimera Techniques", 20th European Rotorcraft Forum, Amsterdam, Netherlands, 1994.

[3] E.P.N. Duque, R. Biswas and R. Strawn, "A Solution Adaptive Structured/Unstructured Overset Grid Flow Solver with Applications to Helicopter Rotor Flows", 13th AIAA Applied Aerodynamics Conference, San Diego, CA, 1995.

[4] J. Ahmad and E.P.N. Duque, "Helicopter Rotor Blade Computation in Unsteady Flows using Moving Embedded Grids", 12th AIAA Applied Aerodynamics Conference, AIAA Paper 94-1922, Colorado, 1994.

[5] R. Stangl and S. Wagner, "Euler Calculation of Flow Field Around a Helicopter Rotor in Forward Flight", 20th European Rotorcraft Forum, Amsterdam, Netherlands, 1994.

[6] J. Ch. Boniface and K. Pahlke, "Calculation of Multi-bladed Rotors in Forward Flight using 3D Euler Methods of DLR and ONERA", 22nd European Rotorcraft Forum, Brighton (UK), 1996.

[7] R. Stangl and S. Wagner, "Euler Simulation of a Helicopter Configuration in Forward Flight using a Chimera Technique", 52nd Forum of the American Helicopter Society, Washington, D.C., 1996.

[8] H. Xu, M. Mamou and M. Khalid, "Numerical Simulation of Flows past Two-bladed Rotors in Forward-flight Conditions", 12th Annual Conference of Computational Fluid Dynamics Society of Canada, Ottawa, May 9-11, 2004

[9] F.X. Caradonna, G.H. Laub and C. Tung, "An experimental investigation of the parallel blade-vortex interaction", NASA-TM-86005, Nov., 1984.

[10] C.L. Chen, W.J. McCroskey and S. Obayashi, "Numerical solution of forward flight rotor flow using an upwind method", J. Aircraft, Vol. 28, June, 1991.

[11] H. Xu, S. Zhang and M. Khalid, "Numerical Simulation of Unsteady Flow past a Four-bladed Helicopter Rotor in Forward Flight" 17th AIAA Computational Fluid Dynamics Conference, 6-9 June 2005, Toronto, Canada.

[12] J.W. Elliott, S.L. Althoff and R.H. Sailey, "Inflow Measurement made with a Laser Velocimeter on a Helicopter Model Forward Flight", NASA Technical Memorandum, 88-B-004, April, 1988.

[13] S. Chaffin and J. Berry, "Navier-Stokes and potential theory solutions for a helicopter fuselage and comparison with experiment", NASA Technical Memorandum 4566, ATCOM Technical Report 94-A-013, June, 1994.

[14] CFD-FASTRAN Software Manual, CFD Research Corporation, Huntaville, AL, 2002.

[15] WIND code, User's Guide, The NPARC Alliance, Sept. 1999.

[16] R. E. Mineck and S. A. Gorton, "Steady and periodic pressure measurements on a generic helicopter fuselage model in the presence of a rotor", NASA/TM-2000-210286.